

High-Resolution Radioluminescence Microscopy of ^{18}F -FDG Uptake by Reconstructing the β -Ionization Track

Guillem Pratx, Kai Chen, Conroy Sun, Marian Axente, Laura Sasportas, Colin Carpenter, and Lei Xing

Department of Radiation Oncology, Stanford University School of Medicine, Stanford, California

Radioluminescence microscopy is a new method for imaging radionuclide uptake by single live cells with a fluorescence microscope. Here, we report a particle-counting scheme that improves spatial resolution by overcoming the β -range limit. **Methods:** Short frames (10 μs –1 s) were acquired using a high-gain camera coupled to a microscope to capture individual ionization tracks. Optical reconstruction of the β -ionization track (ORBIT) was performed to localize individual β decays, which were aggregated into a composite image. The new approach was evaluated by imaging the uptake of ^{18}F -FDG in nonconfluent breast cancer cells. **Results:** After image reconstruction, ORBIT resulted in better definition of individual cells. This effect was particularly noticeable in small clusters (2–4 cells), which occur naturally even for nonconfluent cell cultures. The annihilation and Bremsstrahlung photon background signal was markedly lower. Single-cell measurements of ^{18}F -FDG uptake that were computed from ORBIT images more closely matched the uptake of the fluorescent glucose analog (Pearson correlation coefficient, 0.54 vs. 0.44, respectively). **Conclusion:** ORBIT can image the uptake of a radiotracer in living cells with spatial resolution better than the β range. In principle, ORBIT may also allow for greater quantitative accuracy because the decay rate is measured more directly, with no dependency on the β -particle energy.

Key Words: radionuclide imaging instrumentation; single-cell analysis; microscopy; autoradiography

J Nucl Med 2013; 54:1841–1846

DOI: 10.2967/jnumed.112.113365

Autoradiography is a well-established method for high-resolution imaging of radionuclide probes in tissues. Film and emulsion methods have the highest spatial resolution but poor sensitivity, dynamic range, and quantitative accuracy and require tedious sample preparation (1,2). Other autoradiography methods (e.g., storage phosphor (3), solid-state detection (4,5), gaseous detectors (6), and thin phosphor (7)) have higher sensitivity and dynamic range but spatial resolution worse than 50 μm . Only a few methods have demonstrated the ability to visualize the uptake of radionuclide probes with single-cell resolution. One of these methods uses a β -sensitive avalanche photodiode to measure radionuclide uptake in small groups of cells, cultured in 16 microfluidic chambers (8). An experiment showed that the avalanche photodiode could measure

signal from a single cell in the chamber. Another device, the Micro-Imager, achieved 15- μm spatial resolution for ^{35}S , which was used to detect in situ hybridization in single neurons (9). A third device, the radioluminescence microscope, was developed to visualize radionuclide uptake in live cells during fluorescence microscopy (10). Radioluminescence microscopy can be used to measure fluorescent and radionuclide signals emanating from a collection of living cells, in a relatively short time. Here we propose a new particle-counting scheme for radioluminescence microscopy with higher spatial resolution and, in principle, quantitative accuracy.

The standard radioluminescence microscopy approach uses a scintillator plate, placed in contact with the cells of interest, to convert ionizing radiation from radioactive β decay into visible-range photons detectable with a fluorescence microscope (Fig. 1A). To ensure good contact, the cells are grown such that they adhere to the scintillator plate. The transparency of the plate in the visible range allows for conventional microscopy techniques (e.g., fluorescence and brightfield). Before imaging, the cells are incubated with a radionuclide probe and then washed to remove the excess probe. A radioluminescence image is acquired using a sensitive camera coupled to a high-numerical-aperture microscopy objective (Fig. 1A). A typical image requires an exposure time of several minutes and combines the contributions of thousands of β particles, each emitted with a random energy and direction.

Although radioluminescence microscopy can measure radiotracer uptake with single-cell resolution (10), this single-exposure approach is suboptimal for 2 reasons. First, as each β -particle travels through the scintillator plate, it leaves behind a track of optical photons. Since a β -particle may travel beyond the boundaries of the cell in which it was emitted, it may contribute radioluminescence signal to other surrounding cells, which makes it difficult to distinguish individual cells in the radioluminescence image. Second, the contribution of each individual positron decay event to the total luminescent signal varies greatly because each positron is emitted with a variable amount of kinetic energy and deposits a variable fraction of this energy in the scintillator at a variable depth. The inclusion in the signal of these random quantities results in higher statistical variance.

We report a new image acquisition scheme for radioluminescence microscopy that solves the 2 aforementioned problems. Rather than acquiring a single image with a long exposure time (e.g., 5 min), we take thousands of short frames with high-electron-multiplication gain. With this method, we can visualize the ionization tracks produced by individual β particles as they travel through the scintillator. We trace each track backward to the 2-dimensional location of the corresponding β decay. From the estimated locations of many radioactive decays, we synthesize a composite image that has improved spatial resolution compared with the single-exposure acquisition scheme (Fig. 1B). We have given this particle-counting

Received Sep. 20, 2012; revision accepted Apr. 12, 2013.

For correspondence or reprints contact: Guillem Pratx, 875 Blake Wilbur Dr., MC 5847, Stanford, CA 94305.

E-mail: pratx@stanford.edu

Published online Sep. 3, 2013.

COPYRIGHT © 2013 by the Society of Nuclear Medicine and Molecular Imaging, Inc.

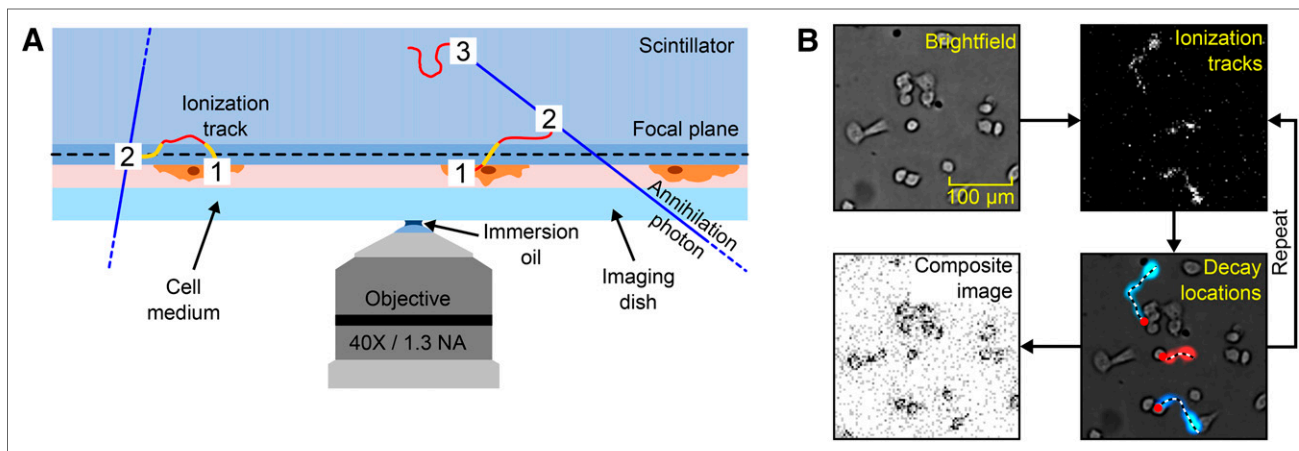


FIGURE 1. Radioluminescence microscopy using ORBIT. (A) Emission of positron from radiotracer bound to cell (1) is followed by positron-electron annihilation (2) and emission of 2 back-to-back 511-keV photons (blue lines), which may interact with electron in scintillator via Compton scatter or photoelectric absorption (3). Energetic charged particles (red lines) propagate through scintillator, producing light, which can be recorded by microscope. Because of shallow depth of field, system is sensitive only to events occurring near focal plane. (Drawing is not to scale: objective's field of view is 1.2 mm). (B) To acquire radioluminescence image with ORBIT, bright-field micrograph is first acquired to delineate cell boundaries. Sequence of short image frames is then acquired with high gain to capture ionization tracks produced by energetic charged particles. Those frames are processed to extract decay locations, which are then aggregated into composite image. (Each decay location is represented as a dot). NA = numerical aperture.

scheme the name *optical reconstruction of the β -ionization track* (ORBIT).

Although in principle similar to existing particle-counting autoradiography systems (5,9), ORBIT can image and reconstruct individual ionization tracks. In this regard, it is comparable to single-molecule fluorescence microscopy methods such as subdiffraction-limit imaging by stochastic optical reconstruction microscopy (11). This method uses bright light pulses to stochastically photoactivate a small number of fluorescent proteins, which are then fluorescently imaged. Because of their sparse distribution, individual activated proteins can be localized with precision greater than the diffraction limit. By repeating this process, different subsets of proteins can be activated and imaged. Similarly, ORBIT exploits the fact that radioactive decay is stochastic, and thus only a small number of randomly distributed ionization tracks are produced within a short time frame. The number of optical photons produced in a scintillator during a single radioactive decay event is large enough to be detected by a sensitive microscope. For instance, the kinetic energy of a positron emitted during the decay of ^{18}F can be as high as 634 keV, which for a scintillator such as CdWO_4 (15 photons/keV) would result in up to 9,500 photons emitted.

MATERIALS AND METHODS

Imaging System

The microscope setup used in this study has been described elsewhere (10). A 40 \times /1.3-numerical aperture oil-immersion objective (UPLFLN40XO; Olympus) was used for all experiments. We estimate that the microscope collects approximately 13% of the photons emitted near the focal plane, based on the objective light collection efficiency (25% for a 1.3 numerical aperture) and transmission (80%), the throughput of the tube lens (80%), and the quantum efficiency of the charge-coupled device (CCD) (80%). The light collection efficiency calculation does not account for the higher index of refraction of the scintillator ($n = 2.3$). Experimentally, we found that the microscope could record 31% of the photons emitted by a bioluminescent light source (Supplemental Fig. 1; supplemental materials are available online at <http://jnm.snmjournals.org>). The discrepancy between these

2 values may be due to camera calibration factors, electron-multiplication gain nonlinearity, and the nonideal behavior of the microscope objective.

Depth-Varying Point-Spread Function

We characterized the depth-varying point-spread function and modulation transfer function of the microscope objective using an analytic model (12). The model accounts for the immersion oil and the index of refraction of the scintillator. Using this model, we computed via convolution the response of the microscope to a small pointlike object placed at different depths. The object was a 3-dimensional gaussian function with a full width at half maximum of 6.5 μm —that is, twice the camera pixel size (with 2 \times 2 binning).

ORBIT Imaging

The general methodology for acquiring an ORBIT image is as follows. We first acquire a sequence of frames with a short exposure time, an electron-multiplication gain of 1,200, and 2 \times 2 binning. The exposure time must be set to maximize the system sensitivity. On the one hand, the exposure should be short enough to avoid spatiotemporal overlap between different ionization tracks. On the other hand, it should be longer than the camera readout time to allow for continuous imaging. For highly radioactive samples, these 2 conditions cannot be simultaneously satisfied; therefore, the exposure should be set to the highest value that causes no overlap between tracks. Typically, this value corresponds to an average of 10 ionization events per frame (Supplemental Fig. 2), but it may vary with the spatial distribution of the activity. Loss of sensitivity due to slow camera readout is spatially uniform. Given the range of camera exposures available (10 μs –10 s), the microscope can image a wide range of radionuclide activities, from 0.2 Bq/ mm^2 to 20 kBq/ mm^2 . For a fixed exposure time, the event rate is also linear with activity concentration (Supplemental Fig. 3).

The automated extraction of β trajectories from the sequence of short frames involves a certain number of image processing steps. Briefly, each frame is first filtered with a gaussian kernel to reduce spatially uncorrelated shot noise. An H-maxima transform is then applied to suppress small local image maxima. The processed image is later segmented using a constant threshold set above the noise floor.

Morphologic operations are also applied to regularize the delineation of the segmented tracks.

For image processing purposes, we distinguish 3 types of ionization tracks. Long tracks ($\leq 500 \mu\text{m}$) are produced by positrons with high initial kinetic energy and are traced backward to the decay origin using a custom algorithm (Fig. 2A). Because the direction of the particle along the track is ambiguous, the origin is defined as the end of the track closest to a cell (segmented from a bright-field micrograph). Shorter tracks are characteristic of positrons that either travel a short distance because of lower kinetic energy or travel orthogonally to the imaging plane (Fig. 2B). These tracks are directly assigned to the nearest cell. Last, annihilation photons are more likely to interact deep in the scintillator plate, away from the focal plane (Fig. 1A). These interactions sometimes appear as a diffuse, out-of-focus luminescence signal and are rejected during image processing (Fig. 2C). A more detailed description of the track reconstruction algorithm is presented as supplemental information.

The final ORBIT image is reconstructed by aggregating the decay locations estimated from the sequence of frames. The resulting image is then filtered with a gaussian kernel to account for the localization uncertainty.

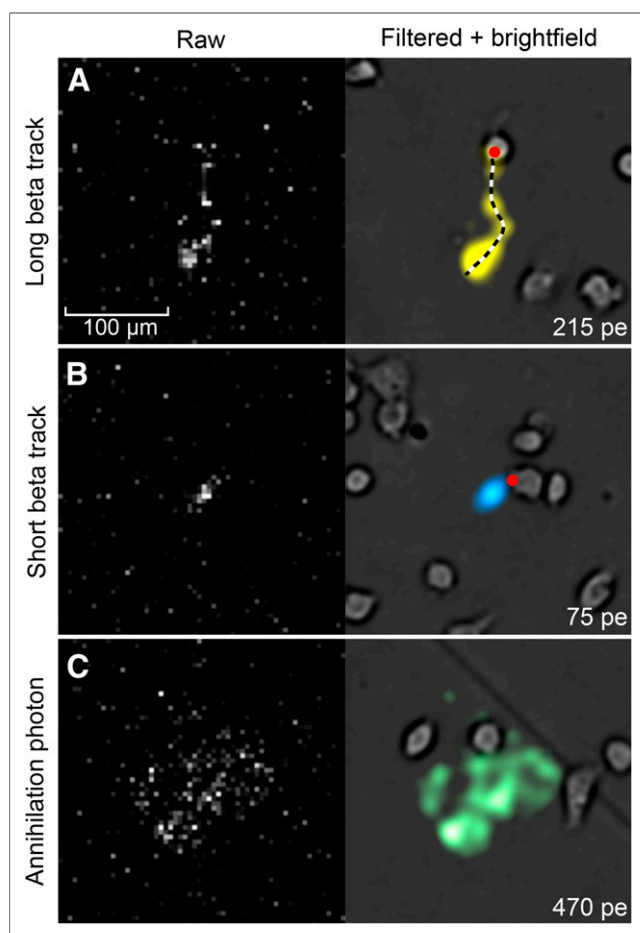


FIGURE 2. Examples of ionization tracks. (A) Long ionization track, originating from cell. Dashed line is estimated positron trajectory. (B) Shorter ionization track, likely produced by low-energy positron or positron traveling orthogonally to imaging plane. Red dot is estimated decay location. (C) Annihilation photon interacting deep in scintillator and producing diffuse, unfocused signal. Such signals are not used in final image. Number of photoelectrons (pe) recorded by CCD sensor for each event is indicated.

Annihilation and Bremsstrahlung Photon Contamination

To evaluate the proportion of events that is produced by secondary annihilation and Bremsstrahlung photons, we imaged the ionization tracks produced by a thin layer of ^{18}F -FDG ($19 \text{ kBq}/\text{mm}^2$) while varying the focal plane depth. For each depth, we counted how many ionization tracks were in focus in 200 sequential images (27-ms exposure). Because the objective has a shallow depth of field, only ionization tracks near the focal plane are in focus. Because of the limited range of positrons, tracks observed deep in the scintillator are attributed to high-energy photons.

Cell Imaging

As a demonstration, we imaged the uptake of ^{18}F -FDG in human breast adenocarcinoma cells and compared it with an optical fluorescent glucose analog, 2-[*N*-(7-nitrobenz-2-oxa-1,3-dioxol-4-yl)amino]-2-deoxyglucose (2-NBDG). We seeded 10^4 MDA-MB-231 cells on a $10 \times 10 \times 0.5 \text{ mm}$ CdWO_4 scintillator plate. The plate was immersed in RPMI 1640 supplemented with 10% fetal bovine serum and 1% penicillin/streptomycin and stored at 37°C in a humidified atmosphere with 5% CO_2 . The next day, the cells were approximately 10% confluent and did not present signs of altered function (Supplemental Fig. 4). After keeping the cells fasting for 30 min in glucose-free RPMI, we incubated them for 1 h at 37°C with ^{18}F -FDG (11 MBq) and 2-NBDG ($100 \mu\text{M}$) and washed them to remove the excess probe.

Imaging was performed by 2 methods. First, a single radioluminescence image was acquired with an exposure time of 5 min and an electron-multiplication gain of 201. Then, a sequence of 6,000 frames was acquired with an exposure time of 50 ms—effectively spanning 5 min—and an electron-multiplication gain of 1,200 and reconstructed into a single image using ORBIT. Image reconstruction took about 8 h using MATLAB (The MathWorks) on a recent computer, with most of the computation spent reconstructing long positron tracks.

RESULTS

The point-spread function and modulation transfer function were found to depend strongly on the depth of the source (Supplemental Fig. 5). The Nyquist frequency for the camera (0.15 cycles/ μm for 2×2 binning) was attenuated by 50% at a $2\text{-}\mu\text{m}$ depth and by 90% at $4 \mu\text{m}$. For a small point-source object, the response of the microscope decreased gradually with depth (Fig. 3), an effect known as optical sectioning. It follows from these results that the sensitive region of the scintillator spans approximately $5 \mu\text{m}$ on either side of the focal plane. Therefore, when an energetic positron intersects the focal plane, the microscope can capture only the portion of its track that is in this sensitive region. The simulation of simple positron trajectories showed that the transition between the 2 regions is gradual (Supplemental Fig. 6). Because of optical sectioning, the microscope captures only a fraction of the total energy deposited by energetic positrons, which can travel up to $500 \mu\text{m}$ in CdWO_4 .

By varying the depth of the focal plane, we estimated that positrons constitute 92% of the events recorded at the scintillator edge (Fig. 4). The event counting rate was 1,010 cps for positrons and 90 cps for annihilation and Bremsstrahlung photons. Positrons rarely traveled more than $20 \mu\text{m}$ from the scintillator edge, highlighting the need for precise focusing to maximize positron sensitivity.

An ORBIT radioluminescence image of cellular ^{18}F -FDG uptake was synthesized from 33,253 events (110.8 cps). As a control, we also imaged a sample not incubated with ^{18}F -FDG and measured a background rate of 1.2 cps, likely caused by cosmic radiation and background noise in the camera. On the basis of the

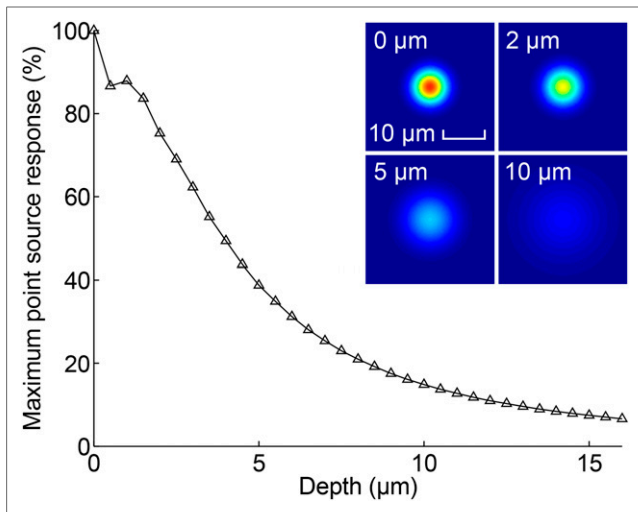


FIGURE 3. Maximum point-source response as function of depth. Maximum response of microscope to small object (gaussian distribution with a full-width half-maximum of $6.5 \mu\text{m}$) placed at various depths was computed using analytic model. Inset shows 2-dimensional point-spread function (depth, 0, 1, 1.5, and $2 \mu\text{m}$).

camera gain and calibration factor, we estimated that single ionization events created between 20 and 1,000 photoelectrons in the CCD sensor, with an average of 390 (Supplemental Fig. 7A). On the basis of the estimated optical sensitivity of the system and the light yield of the scintillator, these correspond to minimum, average, and maximum energy depositions of 10, 200, and 510 keV, respectively. These observed energy depositions reflect the diversity of positron energies and trajectories and represent only ionization occurring within $5 \mu\text{m}$ of the focal plane. This may be why the average measured energy was smaller than the average positron energy for ^{18}F (250 keV).

For both imaging modes, the noise is dominated by shot noise and, for the high-gain acquisition, excess noise factor, with a negligible contribution from dark noise (0.001 electron/pixel/s) and read noise (0.01 electron/pixel at 11 MHz, relative to electron-multiplication gain). On average, a positron produced 0.6 photoelectrons per CCD pixel (before electron-multiplication and analog gain, but after 2×2 pixel binning; Supplemental Fig. 7B). In comparison, a pixel receives approximately 150 photoelectrons for a 5-min exposure. As a result, single ORBIT frames have a low signal-to-noise ratio compared with longer exposures (Supplemental Table 1). Other sources of background signal include Cerenkov luminescence—approximately 1.4 photons per decay for ^{18}F (13)—and scintillator afterglow (e.g., lutetium orthosilicate).

Although isolated cells are clearly distinguishable on the 5-min exposure image (Fig. 5A, red arrows), ORBIT provides better resolution of single cells in small clusters of 2–4 cells (Fig. 3A, yellow arrows). A line profile through the images confirms that peaks and valleys are better defined on the ORBIT image and coincide to a greater degree with the fluorescence image (Fig. 5B; Pearson correlation coefficient, 0.85 vs. 0.67). In contrast, the 5-min-exposure radioluminescence image presents a higher level of background signal between peaks, likely caused by annihilation and Bremsstrahlung photons, and a widening of the peaks, due to positron range blurring. In addition, ORBIT directly counts how many decays occur within each cell, with no dependence on the variable positron energy. Thus, a region-of-interest analysis found

that, on a cell-by-cell basis, 2-NBDG fluorescence was more highly correlated with ^{18}F -FDG uptake measured with ORBIT than with a 5-min exposure (Fig. 5C). A perfect correlation between ^{18}F -FDG and 2-NBDG is not achievable as the 2 probes are not strictly identical: 2-NBDG is degraded after cell internalization, becoming inactive, whereas ^{18}F -FDG accumulates in the cell as FDG-6-phosphate. Physical differences between radionuclide decay and fluorescence emission can also account for discrepancies between the 2 signals.

DISCUSSION

We found that ORBIT could visualize individual decay events and resulting ionization tracks. By processing those ionization tracks, we produced images of the distribution of ^{18}F -FDG in living cells with spatial resolution greater than the positron range. Whereas a single-exposure radioluminescence image has arbitrary camera units, an ORBIT image has units of counting rate. In principle, a particle-counting approach such as ORBIT should be more quantitative than an integrating approach. That may be why ORBIT images provided measurements of ^{18}F -FDG uptake in single cells that presented a stronger correlation to the uptake of a fluorescent glucose analog. A precise comparison between the 2 approaches will be the aim of future work.

We also found that because of the shallow depth of field of the objective, imaging of ionizing events is restricted to a $10\text{-}\mu\text{m}$ -thick slab centered on the focal plane. This feature of the microscope allowed us to better discriminate between positrons, which travel short distances, and secondary photons, which interact more deeply in the scintillator.

ORBIT works best for nonconfluent cell cultures because each positron track can reliably be assigned to a cell delineated from a bright-field microscopy image. ORBIT is generally able to distinguish individual cells in small clusters (2–4 cells) that naturally occur during cell growth (Fig. 3A, yellow arrows). However, for more confluent cell distributions such as tissue sections, the bright-field image is less useful for estimating the positron direction along the track because more than one cell may be equally close to the

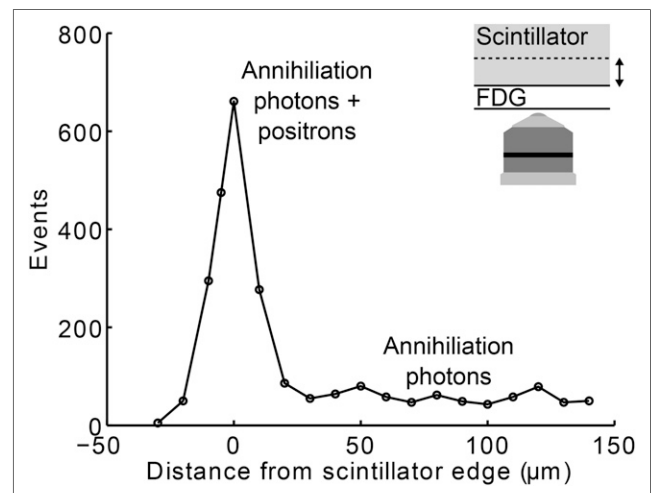


FIGURE 4. Annihilation and Bremsstrahlung photon contamination. A thin layer of ^{18}F -FDG ($19 \text{ kBq}/\text{mm}^2$) placed between scintillator and imaging dish was imaged by acquiring 200 frames (3-ms exposure). Events in focus—that is, that displayed high-frequency features—were counted at various focal depths.

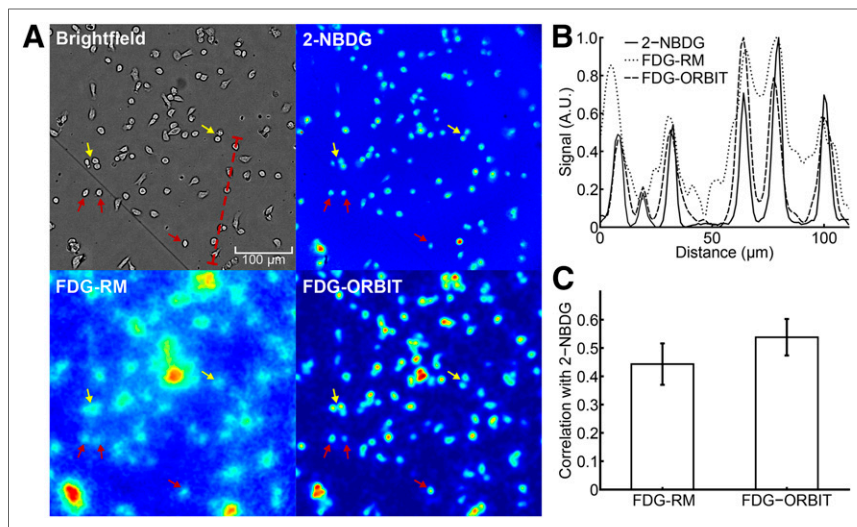


FIGURE 5. Radioluminescence microscopy of ^{18}F -FDG uptake. Human breast cancer cells (MDA-MB-231) were deprived of glucose for 1 h, incubated for 1 h with ^{18}F -FDG (11 MBq) and 2-NBDG (100 μM), and then washed. (A) Bright-field (scale bar, 200 μm), fluorescence (2-NBDG), single-exposure radioluminescence microscopy (FDG-RM), and ORBIT (FDG-ORBIT). Objective is 40 \times /1.3 numerical aperture. (B) Radioluminescence and fluorescence intensity shown along line profile (red dashed line in A). (C) Correlation between cellular uptake of 2-NBDG and ^{18}F -FDG, where ^{18}F -FDG uptake was measured with conventional radioluminescence microscopy (FDG-RM) or ORBIT (FDG-ORBIT). Cellular uptake was computed by drawing circular region of interest around each cell on bright-field image.

ionization track. This is unfortunate because dense cell distributions are more representative of physiologic conditions. ORBIT can be adapted to imaging dense tissue in several ways. As the positron slows down, it becomes more ionizing and its ionization track becomes brighter. Furthermore, as the positron moves away from the focal plane, the ionization track becomes defocused. These properties may help determine the direction of the positron along its track. Alternatively, long ionization tracks may also be discarded in favor of shorter tracks that are easier to localize. Tissue dissociation techniques may also allow dense tissues to be physically separated for imaging (14).

The ORBIT method can readily be extended to dynamic studies. Short frames can be acquired for the desired duration of the study, retrospectively gated into time intervals, and independently reconstructed. However, the use of the bright-field image to delineate cells is not optimal in the presence of background activity. Positrons emitted from a free radionuclide probe will produce ionization tracks that should not be associated with a cell. Thus, to avoid bias, β particles should be localized without using the bright-field image when significant activity is present in the background.

Highly sensitive CCD cameras with high internal gain, comparable to the one used in this work, have in recent years found application in high-resolution SPECT imaging (15–18). These SPECT systems image the ionization track produced by low-energy γ rays interacting in a thin scintillator screen. Similar to our work, they apply image-processing algorithms to extract the position and energy of each individual γ -ray interaction. Such an imaging scheme enables spatial resolution on the order of 50–70 μm , much higher than conventional SPECT systems. In a similar fashion, a digital autoradiography system was recently developed using a high-efficiency CCD sensor (19). By placing the tissue of

interest in direct contact with the CCD, this system can directly visualize the trajectories of positrons entering the silicon detector. The system achieved a spatial resolution of 86 μm when imaging ^{18}F in a 100- μm -thick tissue section. However, it is not compatible with live cell imaging because the CCD sensor must be cooled to very low temperatures. Furthermore, unlike radioluminescence microscopy, it is unable to image the tissue optically.

CONCLUSION

Because of limited spatial resolution, autoradiography and other methods can measure the uptake of a radiotracer only in a relatively large cell population. In contrast, radioluminescence microscopy is able to measure radiotracer uptake with single-cell resolution, in the familiar environment of a fluorescence microscope, using fluorescent probes to highlight biochemical features of interest. Dynamic studies can also shed light on radiotracer kinetics in vitro and at the single-cell level. The ORBIT scheme presented here makes those single-cell measurements more accurate with no increase in imaging time or hardware complexity. Future work will focus on applying this approach for imaging denser cell distributions such as tissue sections.

DISCLOSURE

The costs of publication of this article were defrayed in part by the payment of page charges. Therefore, and solely to indicate this fact, this article is hereby marked “advertisement” in accordance with 18 USC section 1734. This work was supported by the National Institutes of Health under grant NIH ICMIC P50CA114747 and by the Department of Defense under grant W81XWH-11-1-0070. The Olympus Corporation provided the LV200. No other potential conflict of interest relevant to this article was reported.

ACKNOWLEDGMENTS

The authors gratefully acknowledge the help of the Stanford nuclear medicine technologists, Stanford postdoctoral fellows Irfan Ali-Khan and Steven Sensarn for assistance with the instrumentation, and the Stanford Small-Animal Imaging and Radiochemistry Facility.

REFERENCES

1. Kubota R, Yamada S, Kubota K, Ishiwata K, Tamahashi N, Ido T. Intratumoral distribution of fluorine-18-fluorodeoxyglucose in vivo: high accumulation in macrophages and granulation tissues studied by microautoradiography. *J Nucl Med.* 1992;33:1972–1980.
2. Nielsen JL, Halkjær Nielsen P. Advances in microscopy: microautoradiography of single cells. *Methods Enzymol.* 2005;397:237–256.
3. Johnston RF, Pickett SC, Barker DL. Autoradiography using storage phosphor technology. *Electrophoresis.* 1990;11:355–360.
4. Ott RJ, Macdonald J, Wells K. The performance of a CCD digital autoradiography imaging system. *Phys Med Biol.* 2000;45:2011–2027.

5. Mettievier G, Montesi MC, Russo P. First images of a digital autoradiography system based on a Medipix2 hybrid silicon pixel detector. *Phys Med Biol*. 2003;48:N173–181.
6. Charpak G, Dominik W, Zaganidis N. Optical imaging of the spatial distribution of beta-particles emerging from surfaces. *Proc Natl Acad Sci USA*. 1989;86:1741–1745.
7. Chen L, Gobar LS, Knowles NG, Liu Z, Gmitro AF, Barrett HH. Direct imaging of radionuclide-produced electrons and positrons with an ultrathin phosphor. *J Nucl Med*. 2008;49:1141–1145.
8. Vu NT, Zeta T, Comin-Anduix B, et al. A β -camera integrated with a microfluidic chip for radioassays based on real-time imaging of glycolysis in small cell populations. *J Nucl Med*. 2011;52:815–821.
9. Lanière P, Charon Y, Dumas S, et al. HRR1: a high resolution radioimager for fast, direct quantification in in situ hybridization experiments. *Biotechniques*. 1994;17:338–345.
10. Pratz G, Chen K, Sun C, et al. Radioluminescence microscopy: measuring the heterogeneous uptake of radiotracers in single living cells. *PLoS ONE*. 2012;7:e46285.
11. Rust MJ, Bates M, Zhuang X. Sub-diffraction-limit imaging by stochastic optical reconstruction microscopy (STORM). *Nat Methods*. 2006;3:793–795.
12. Gibson SF, Lanni F. Experimental test of an analytical model of aberration in an oil-immersion objective lens used in three-dimensional light microscopy. *J Opt Soc Am A*. 1992;9:154–166.
13. Mitchell GS, Gill RK, Boucher DL. In vivo Cerenkov luminescence imaging: a new tool for molecular imaging. *Phil Trans R Soc A*. 2011;369:4605–4619.
14. Hedley DW. Flow cytometry using paraffin-embedded tissue: five years on. *Cytometry*. 1989;10:229–241.
15. Meng LJ, Fu G, Roy EJ, Suppe B, Chen CT. An ultrahigh resolution SPECT system for I-125 mouse brain imaging studies. *Nucl Instrum Meth A*. 2009;600:498–505.
16. Soesbe TC, Lewis MA, Slavine NV, Richer E, Bonte FJ, Antich PP. High-resolution photon counting using a lens-coupled EMCCD gamma camera. *IEEE Trans Nucl Sci*. 2010;57:958–963.
17. Nagarkar VV, Shestakova I, Gaysinskiy V, Singh B, Miller BW, Bradford Barber H. Fast x-ray/ γ -ray imaging using electron multiplying CCD-based detector. *Nucl Instrum Meth A*. 2006;563:45–48.
18. Miller BW, Barrett HH, Furenlid LR, Bradford Barber H, Hunter RJ. Recent advances in BazookaSPECT: real-time data processing and the development of a gamma-ray microscope. *Nucl Instrum Meth A*. 2008;591:272–275.
19. Peng Q, Holland SE, Choong WS, Budinger TF, Moses WW. Real-time quantitative ex vivo direct autoradiography with 10 μ m pixel resolution. *Conf Proc IEEE Eng Med Biol Soc*. 2011;6273–6276.

Erratum

In the article “Assessment of Treatment Response in Patients with Glioblastoma Using *O*-(2-¹⁸F-Fluoroethyl)-L-Tyrosine PET in Comparison to MRI,” by Galldiks et al. (*J Nucl Med*. 2012;53:1048–1057), the abstract mistakenly stated, “Receiver-operating-characteristic analysis showed that a decrease of the TBR(max) between FET-1 and FET-2 of more than 20% predicted poor survival. . . .” However, such a decrease in fact predicted favorable survival, not poor survival. The authors regret the error.